7-25-2016

Engineered surfaces to control secondary electron emission for multipactor suppression

James M. Sattler
Air Force Institute of Technology

Ronald A. Coutu Jr.
Marquette University, ronald.coutu@marquette.edu

Robert A. Lake
Air Force Institute of Technology

Tod V. Laurvick
Air Force Institute of Technology

Recommended Citation

Sattler, James M.; Coutu, Ronald A. Jr.; Lake, Robert A.; and Laurvick, Tod V., "Engineered surfaces to control secondary electron emission for multipactor suppression" (2016). *Electrical and Computer Engineering Faculty Research and Publications*. 419.
https://epublications.marquette.edu/electric_fac/419

Electrical and Computer Engineering Faculty Research and Publications/College of Engineering

2016 IEEE National Aerospace and Electronics Conference (NAECON) and Ohio Innovation Summit (OIS), (July, 2016). DOI. This article is © Institute of Electrical and Electronic Engineers (IEEE) and permission has been granted for this version to appear in e-Publications@Marquette. Institute of Electrical and Electronic Engineers (IEEE) does not grant permission for this article to be further copied/distributed or hosted elsewhere without the express permission from Institute of Electrical and Electronic Engineers (IEEE).

Contents

Engineered surfaces to control secondary electron emission for multipactor suppression

James M. Sattler
Department of Electrical and Computer Engineering, Air Force Institute of Technology, Wright Patterson AFB, OH
Ronald A. Coutu
Department of Electrical and Computer Engineering, Air Force Institute of Technology, Wright Patterson AFB, OH
Robert A. Lake
Department of Electrical and Computer Engineering, Air Force Institute of Technology, Wright Patterson AFB, OH
Tod Laurvick
Department of Electrical and Computer Engineering, Air Force Institute of Technology, Wright Patterson AFB, OH

Abstract:

A significant problem for space-based systems is multipactor - an avalanche of electrons caused by repeated secondary electron emission (SEE). The consequences of multipactor range from altering the operation of radio frequency (RF) devices to permanent device damage. Existing efforts to suppress multipactor rely heavily on limiting power levels below a multipactor threshold.[1] This research applies surface micromachining techniques to create porous surfaces to control the secondary electron yield (SEY) of a material for multipactor suppression. Surface characteristics of interest include pore aspect ratio and density. A discussion is provided on the advantage of using electroplating (vice etching) to create porous surfaces for studying the relationships between SEY and pore aspect ratio & density (i.e. porosity). Preventing multipactor through SEY reduction will allow power level restrictions to be eased, leading to more powerful and capable space-based systems.

SECTION I. Introduction

Multipactor is an explosive increase in the number of free electrons (often referred to as an "electron avalanche") caused by repeated Secondary Electron Emission (SEE) stimulated by an RF signal in a vacuum. It can occur over a wide range of frequencies (MHz to GHz) and presents a host of problems for RF circuits including noise enhancement, cavity detuning, RF power dissipation, and localized heating.[2,3] The latter may lead to melting of components, cracking of RF ceramic windows or vacuum discharge, all of which can render the system inoperable.[2,3] Interest in useful applications for multipactor has existed since multipactor was first discovered in 1934 by P.T. Farnsworth, who attempted to use the phenomenon to amplify signals for television camera tubes.[4] However, the vast majority of multipactor research is focused on suppression.[3] The primary scientific and engineering communities concerned with multipactor are those involved with vacuum electronic devices (VEDs), space-based systems, and particle accelerators.[5]

A. Types of Multipactor

Multipactors are broadly categorized as one of two types: two-surface (metallic), and single-surface (dielectric). The fundamental difference in these types is the orientation of the RF field. Two-surface multipactor involves an RF electric field oriented perpandiculer to the two metallic surfaces. The RF field accelerates vacuum electrons into the metallic surfaces causing repeated SEE in synchronsim with the RF signal phase (see Fig. 1). By contrast, single-surface multipactor involves an RF electric field oriented parallel to a positively-charged dielectric. The static electric field associated with the dielectric's positive charge accelerates vacuum electrons into the dielectric surface resulting in repeated SEE (see Fig. 2). This research effort is principally focused on suppressing two-surface multipactors, although we believe the results can also be applied to single-surface multipactors. The seed electron can originate from a variety of sources including field emission or photoelectric emission from a sidewall, electrons native to the space environment, or an electron cascade produced by a cosmic ray.[5,6]

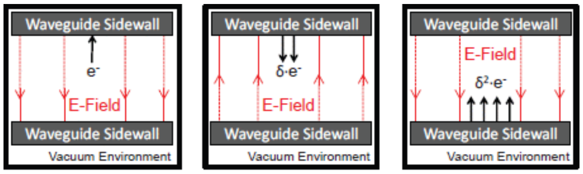

***1.** A seed electron is accelerated by an RF field into a sidewall.*

***2.** The impact causes δ secondary electrons to be emitted which accelerate toward the opposite sidewall due to the RF field reversal.*

***3.** The impact of the δ secondaries causes δ·δ secondaries to be emitted. The process continues creating an avalanche of electrons.*

Fig. 1. Illustration of the recurring process for a two-surface, first-order multipactor.

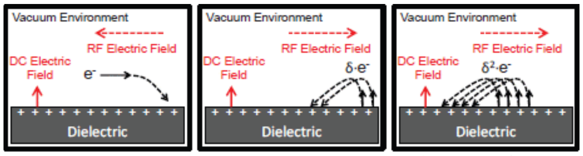

***1.** A seed electron is accelerated by both an applied RF electric field and a DC electric field which causes the seed electron to impact the dielectric.*

***2.** The impact causes δ secondary electrons to be emitted which gain energy from the RF electric field while accelerating back towards the dielectric.*

***3.** The impact of the δ secondaries causes δ·δ secondaries to be emitted. The process continues creating an avalanche of electrons (regardless of the RF field direction).*

Fig. 2. Illustration of the recurring process for a single-surface multipactor.

B. Multipactor Suppression

Two primary physical processes govern multipactor: electron transport and population growth. Multipactor suppression sterns from controlling the factors that influence these processes. Fig. 3 illustrates the relationships between a variety of suppression techniques that have been researched and the factors and processes they seek to affect. The majority of multipactor suppression research has focused on geometrical modifications, conditioning, power level restrictions, and surface treatments. Geometrical modifications involve changing the physical layout of the RF component (e.g. electrode seperation or RF window location) to impose unfavorable multipactor conditions. Although geometrical modifications provide the simplest and most effective suppression technique, they are not always possible given the operating requirements of a particular RF circuit. Conditioning involves initiating a multipactor and using the electron avalanche to remove adsorbed gas from the emitting surfaces. As these gases are removed, the Secondary Electron Yield (SEY) of the emitting surfaces is reduced causing the multipactor to quench itself.[2,7] Unfortunately, conditioning is a lengthy process and does not always result in SEY reductions.[2,8] Power level restrictions provide a more systematic approach to multipactor suppression. This method involves limiting the RF power to remain below the multipactor threshold. Although this method has proven effective during the last 20 years, it is very time-intensive owing to the iterative nature of design-and-test. Furthermore, modern multicarrier communication satellites are proving difficult for determining peak power levels, leading to overly conservative designs.[9] Surface treatments involve directly altering the emitting surfaces (i.e. cleaning, coating, or reshaping) to reduce SEY.[7] As shown in Fig. 3, an advantage to using surface treatments is their ability to influence both SEY and emission angle.

Multipactor suppression using engineered surfaces falls under the category of surface treatments. Historically, the vast majority of research into surface treatments has focused on coating the emitting surfaces with low-SEY materials. Unfortunately, surface coatings are plagued by degradation over time [2]. Alternatively, a surface treatment method that reduces SEY by reshaping the surface to recapture emitted electrons would be immune to such degradation. Interestingly, it has long been understood that roughened surfaces have a lower SEY than smooth surfaces of identical material.[10] But only recently has the use of modern surface engineering techniques received attention as a possible method for controlling SEE.[11,12] Fig. 4 illustrates how an engineered surface can control SEE by providing opportunities for secondary electrons to be recaptured. An advantage of this approach is the ability to combine surface treatment techniques such as coating an engineered surface with a low-SEY material.[12] An engineered surface method would also provide relief to overly conservative power level restrictions by reducing SEY on all emitting surfaces within the RF device. However, because this approach is relatively new and unstudied, more research is needed to prove the concept, determine optimum engineered surfaces, and characterize their impact to RF device performance.

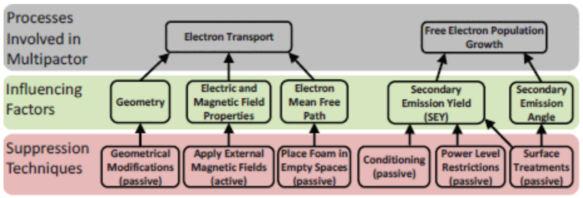

Fig. 3. Illustration of the relationships between multipactor suppression techniques and the multipactor process they disrupt.

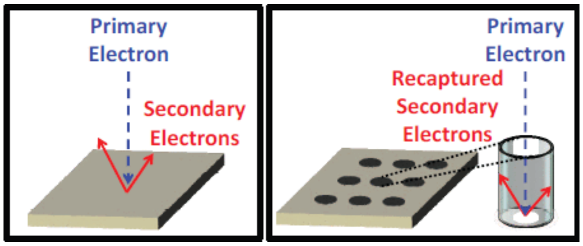

Fig. 4. Illustration of how engineered surfaces can control secondary electron emission (SEE): SEE from a smooth surface (left); reduced SEE from an engineered porous surface (right).

SECTION II. SEY Model for a Porous Surface

Essential to determining optimum engineered surface designs for multipactor suppression is the development of an accurate model for predicting the SEY of an engineered surface. A porous surface was chosen because of its simplicity and ease of fabrication. Fig. 5 shows the geometry used to model the SEY of a porous surface which was previously used by Ye *et al*. in 2013.[11] The subsequent derivation closely follows the derivation provided by Ye *et al*. with two notable distinctions. First, we do not make the assumption that all elastic and inelastic backscattered electrons have a probability of escaping a pore that is equal to one. Instead we avoid distinguishing true secondary electrons from backscattered primaries, preferring to model the total SEY (symbolized by σ). Second, we do not assume that the total SEY of the pore bottoms will be equal to the total SEY of the non-pore regions (see Fig. 5). Fig. 6 illustrates why this is a poor assumption by showing a scanning electron microscope (SEM) image of pores fabricated by Ye *et al*. Clearly evident in Fig. 6 is the difference in roughness between the bottom of a pore and the regions between pores. Consequently, we maintain separate variables for those parameters, namely $\sigma_{\text{pore}-\text{bottom}}$ and $\sigma_{\text{non}-\text{pore}}$. Returning to Fig. 5, the two primary parameters of significance are the pore density (hereto called "Porosity"), defined as

$$Porosity = \frac{Surface\ Area\ of\ Pores}{Total\ Surface\ Area} \tag{1}$$

and the pore aspect ratio, defined as

$$A_R = \frac{H}{2R} \tag{2}$$

where H is the pore height and R is the pore radius. Assuming all incident electrons impact the surface with normal incidence, the SEY of the entire sample can be determined using a weighted average that combines the SEY of the regions of pores with the SEY of the non-pore regions. Mathematically, this weighted average is

$$\sigma_{\text{sample}} = (1 - \text{Porosity})(\sigma_{\text{non}-\text{pore}}) + \text{Porosity}(\sigma_{\text{pore}}), \tag{3}$$

where σ_{pore} is the total yield of electrons exiting the pore. We will treat σnon-pore as a fundamental material parameter that can be measured. However, σpore can be broken down further because it depends on two factors: (1) the SEY of the bottom of the pore and (2) the likelihood that electrons emitted from the bottom of the pore will escape (i.e. will not impact the sidewall). Mathematically, this becomes

$$\sigma_{\text{pore}} = \sigma_{\text{pore}-\text{bottom}}\left(P_{\text{escape}}\right),$$

(4)

where P_{escape} is the probability of an emitted or backscattered electron escaping the pore. We now treat $\sigma_{\text{pore-bottom}}$ as a fundamental material parameter that can be measured and focus on P_{escape} which can be broken down further. The right side of Fig. 5 shows the 2D geometry for a single pore that is useful for determining P_{escape}. The variable F is a horizontal position factor that ranges in value from zero (representing an incident electron impact at the left wall edge) to one (representing an incident electron impact at the right wall edge). Applying basic trigonometry to Fig. 5, the maximum emission angles that allow electrons to escape are,

$$\theta_1 = \tan^{-1}\left(\frac{F(2R)}{H}\right) \text{ and } \theta_2 = \tan^{-1}\left(\frac{2R(1-F)}{H}\right).$$

(5)

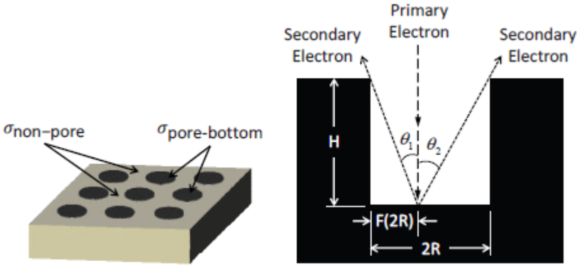

Fig. 5. Porous surface geometry used to develop a SEY model: 3-D model (left); pore cross-section geometry borrowed from ye *et al.*[11] (right).

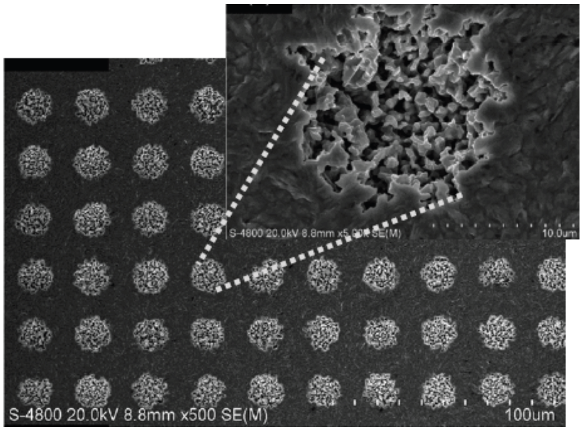

Fig. 6. Scanning electron microscope (SEM) images of micro-scale pores created by ye *et al*. Using a silver etch process.[11]

Substituting (2) into the above equations yields

$$\theta_1 = \tan^{-1}\left(\frac{F}{A_R}\right) \text{ and } \theta_2 = \tan^{-1}\left(\frac{1-F}{A_R}\right).$$

(6)

A reasonable assumption is now made that electron emission toward the left wall is equally as probable as electron emission toward the right wall. This provides,

$$P_{escape} = \frac{1}{2} P_{escape\ left} + \frac{1}{2} P_{escape\ right} \tag{7}$$

where $P_{\text{escape left}}$ is the probability that the emission angle is between 0° (i.e. perfectly backscattered) and θ_1, and $P_{\text{escape right}}$ is the probability that the emission angle is between 0° and θ_2. We now apply the well-documented understanding that the angular distribution of secondary electrons closely follows the cosine function.[13] Mathematically, this is

$$f_{\theta\ emission} = \cos(\theta_{emission}) \tag{8}$$

where θ_{emission} is defined relative to the normal (i.e. $\theta_{\text{emission}} = 0°$ represents emission perpendicular to the emitting surface). Applying the definition of a probability density function provides

$$P(0 < \theta_{emission} < \theta_0) = \int_0^{\theta_0} \cos(\theta_{emission})\, d\theta = \sin\theta_0 \tag{9}$$

Applying the above result to (7) provides,

$$P_{escape} = \frac{1}{2}\sin\theta_1 + \frac{1}{2}\sin\theta_2 \tag{10}$$

Finally, substituting (6) into (10) provides a mathematical expression for the probability of an emitted or backscattered electron escaping the pore.

$$P_{escape} = \frac{1}{2}\sin\left[\tan^{-1}\left(\frac{F}{A_R}\right)\right] + \frac{1}{2}\sin\left[\tan^{-1}\left(\frac{1-F}{A_R}\right)\right] \tag{11}$$

A limitation of (11) is its dependence on the ideal pore geometry shown in Fig. 5. However, as Porosity → 1, the ideal pore geometry breaks down because the pores begin to overlap which removes segments of the pore sidewalls. Fig. 7 shows the maximum valid porosity for two pore layout patterns of interest. Applying (1) to the geometries shown in Fig. 7 provides the following ranges of valid porosity values: 0 ≤ Porosity ≤ 0.785 for square layouts; 0 ≤ Porosity ≤ 0.907 for close-packed layouts.

Equation (3), expanded by substitutions of (4) and (11), provides a useful model for analyzing the roles played by porosity and aspect ratio for controlling SEY. Fig. 8 shows the inverse linear relationship between total SEY and porosity for the specific values of $\sigma_{\text{non-pore}} = 1.4$, $\sigma_{\text{porr-bottom}} = 1.3$, and aspect ratio = 0.5. Because symmetry exists for the ideal 2-D pore geometry shown in Fig. 5 (right), the model's results for electrons incident on the left half of the pore mirror the results for electrons incident on the right half of the pore. This is why lines for $\mathrm{F} = 0.667$, 0.833, and 0.99 are not shown in Fig. 8 — they would simply overlay the curves for $F = 0.333$, 0.167, and 0.01. Another noteworthy feature from Fig. 8 is the increasing slope magnitude as F decreases from 0.5 to 0.01. This is logical because primary electron impacts near a pore sidewall have a greater probability of recapture (i.e. lower P_{escape}) than primary electron impacts near the center of the pore.

The negative slope of the lines in Fig. 8 illustrate the usefulness of maximizing porosity in order to minimize total SEY. Of course this inverse relationship is logical because the premise of this research is based on the idea that adding surface features (i.e. increasing porosity) will reduce SEY. Although the lines shown in Fig. 8 are based on arbitrary values of $\sigma_{\text{non-pore}}$ and $\sigma_{\text{pore-bottom}}$, further analysis can identify the relationship needed between $\sigma_{\text{non-pore}}$ and $\sigma_{\text{pore-bottom}}$ to maintain negative slopes. Treating porosity as the independent variable, (3) can be rewritten in slope-intercept form $(y = mx + b)$ as,

$$\sigma_{sample} = \left[\sigma_{pore} - \sigma_{non-pore}\right] Porosity + \sigma_{non-pore} \tag{12}$$

Substituting (4) into (12) we can see that the slope is negative when

$$\sigma_{non-pore} > \sigma_{pore-bottom}\left(P_{escape}\right) \tag{12}$$

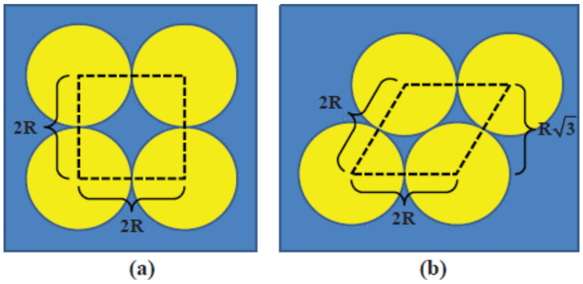

Fig. 7. Maximum porosity achievable without sidewall overlapping for designs involving (a) Square layout and (b) Close-packed layout.

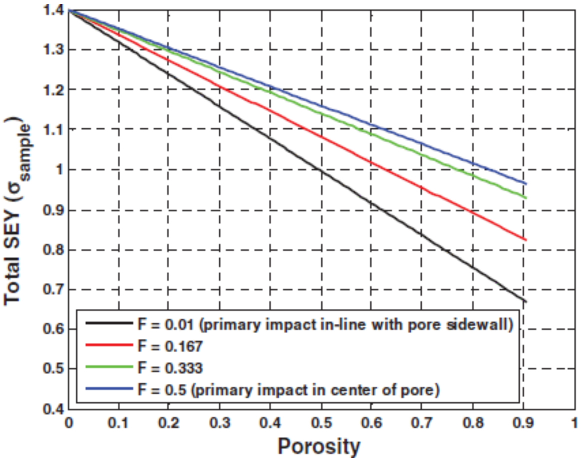

Fig. 8. Total secondary electron yield (SEY) dependence on porosity for the proposed model (3) of a close-packed layout with $\sigma_{\text{non-pore}} = 1.4, \sigma_{\text{pore-bottom}} = 1.3$, and Aspect Ratio $(\mathrm{A_R}) = 0.5$.

Noting that P_{escape} is a probability with range $0 < P_{\text{escape}} < 1$, it becomes clear that the slope is guaranteed to remain negative as long as $\sigma_{\text{non-pore}} > \sigma_{\text{pore-bottom}}$. To better illustrate this concept, we return to the 3-D illustration in Fig. 5 (left) and assume $\sigma_{\text{non-pore}} < \sigma_{\text{pore-bottom}}$. For such surface, an increase in porosity results in trading low-SEY non-pore surface for higher-SEY pore-bottom surface. With the overarching goal of reducing SEY, one can see which this is an undesirable trade. Thus, maintaining $\sigma_{\text{non-pore}} \geq \sigma_{\text{pore-bottom}}$ becomes an important design consideration for optimizing a porous surface to reduce SEY.

Fig. 9 shows the inverse non-linear relationship between total SEY and aspect ratio for a surface porosity = 0.5 and the same values of F, $\sigma_{\text{non-pore}}$, and $\sigma_{\text{pore-bottom}}$ previously used in Fig. 8. Evident in Fig. 9 is the trend that increasing aspect ratio decreases total SEY according to a non-linear “diminishing return” behavior. Thus, pursuing higher and higher aspect ratios to reduce SEY is a misguided objective. This conclusion fits nicely with two other design considerations: (1) as aspect ratio increases, fabrication difficulty increases; (2) increasing the aspect ratio of surface features inside an RF device can negatively affect the device's ability to propagate RF waves.

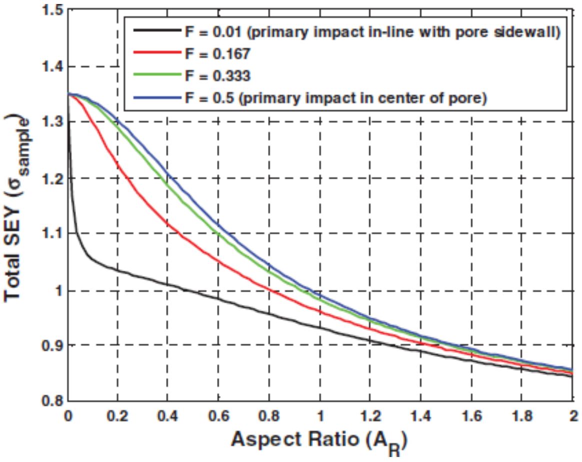

Fig. 9. Total secondary electron yield (SEY) dependence on aspect ratio for the proposed model (3) with $\sigma_{\text{non-pore}} = 1.4, \sigma_{\text{pore-bottom}} = 1.3$, and porosity = 0.5).

The following list provides a summary of noteworthy porous surface design rules taken from the preceding analysis.

1. Restrict porosity to values below the threshold for overlapping pores (i.e. Porosity < 0.785 for square layouts and Porosity < 0.907 for close-packed layouts).
2. Maintain $\sigma_{\text{non-pore}} \geq \sigma_{\text{pore-bottom}}$ to ensure an increase in porosity causes a decrease in SEY.
3. Maximize porosity to minimize SEY.
4. Increasing aspect ratio will reduce SEY but the reductions decrease as aspect ratio increases (i.e. there is a "diminishing return").
5. A critical parameter for low porosity surfaces is $\sigma_{\text{non-pore}}$; a critical parameter for high porosity surfaces is $\sigma_{\text{pore-bottom}}$.

SECTION III. Designs and Fabrication

Fig. 10 shows a matrix of six designs that will be used to experimentally validate the previous SEY model and the aforementioned design rules. The range of sample porosity (0.13 to 0.91) will provide a large contrast for the designed experiment, increasing confidence in the results. As previously mentioned, the range of sample aspect ratio is restricted by fabrication limitations on pore height. For example, achieving an aspect ratio of 0.38 for 16μm diameter pores requires a pore height of 6μm. For pore fabrication, electroplating was chosen as an alternative to the etch-based process used by Ye *et al*.[11] This was done to create smoother pores that more accurately resemble the ideal pore geometry shown in Fig. 5. Such pore accuracy is important for experimentally validating the proposed model. Fig. 11 shows the process for fabricating micro-scale porous surfaces using photolithography and electroplating. A 3 inch silicon wafer with a 500 nm silicon nitride isolation layer was used as a substrate for this fabrication process. The most important features in this process are the pillars of photoresist that act as a mold, around which the metal is electroplated. The primary requirement is a patterned photoresist that is taller than the pore height. Although there is interest in studying a variety of materials used in RF devices (silver, copper, nickel, stainless steel), gold was selected for this initial study because it has well-documented SEY curves, was readily available for electroplating, and has been shown by Nistor *et al*. to be a good candidate for multipactor suppression treatments.[12]

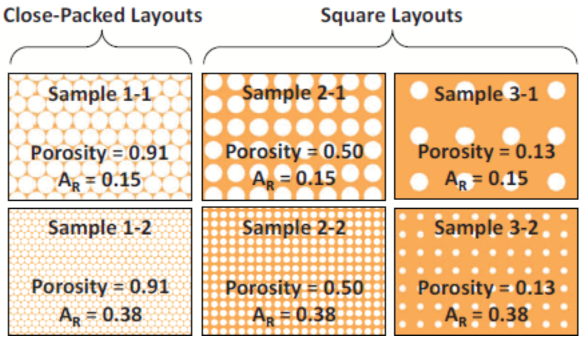

Fig. 10. Designs for studying the influence porosity and aspect ratio have on secondary electron yield at micrometer scales; the pore diameters are 40μm (top row) and 16μm (bottom row).

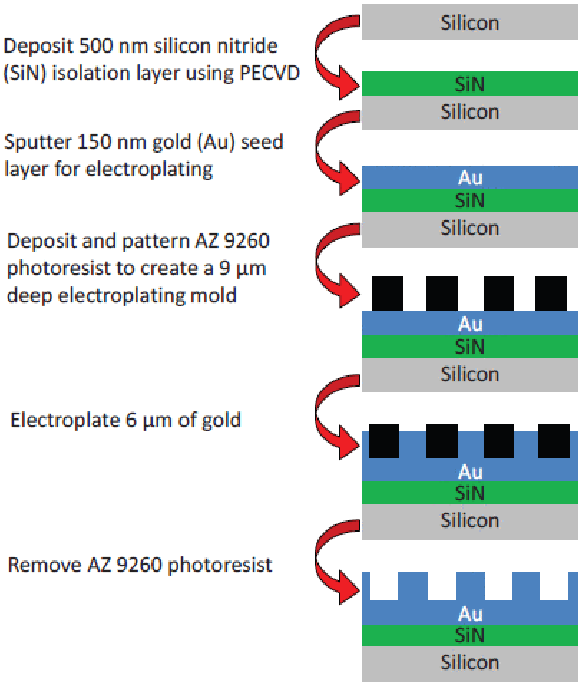

Fig. 11. Process for fabricating gold micro-scale porous surfaces using electroplating.

SECTION IV. Results and Discussion

Fabrication of the gold micro-scale porous surfaces was largely successful. Sample characterization was performed with a profilometer and Scanning Electron Microscope (SEM). The average pore height was measured to be $5.6\mu\mathrm{m}$. Fig. 12 shows SEM images of Sample 3–2 and illustrates the excellent pattern uniformity and pore yield obtained through electroplating. The benefit of electroplating is clearly visible by the smooth sidewalls and bottoms of the pores which stand in stark contrast to the pores shown in Fig. 6. The primary fabrication challenge was maintaining the pore diameter specified in the designs. The pores in Fig. 12 were designed to have $16\mu\mathrm{m}$ diameters. The shrinkage is caused by processing of the patterned photoresist pillars — specifically, the use of an O_2 plasma to clean the wafer prior to electroplating. This shrinkage is somewhat unavoidable but will be accounted for in future design-fabrication cycles.

There was some concern that residual photoresist or other materials used during the fabrication process might be present at the bottoms of the pores. Such material would pose a significant problem during follow-on SEY measurements as it could skew the SEY results and invalidate the measurements. Consequently, an energy dispersive X-ray spectroscopy (EDS) system associated with the SEM was used to characterize the physical elements present in Sample 3–1. Various surface locations were analyzed including near the center of a pore, the pore sidewalls, and in the non-pore regions. Results for all EDS measurements were identical and indicated that gold was the only element present.

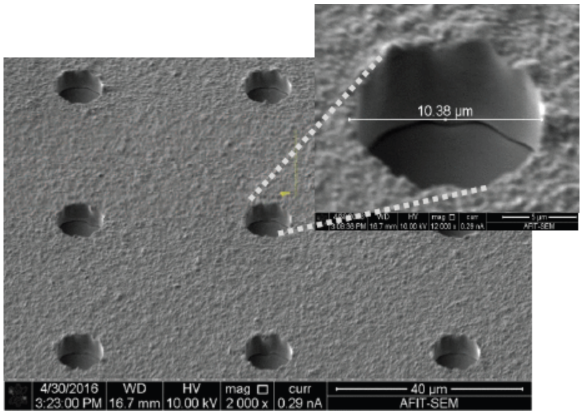

Fig. 12. Scanning electron microscope (SEM) images of pores created in this effort using a gold electroplating process.

An additional fabrication challenge was uncovered during characterization of the close-packed designs. Fig. 13 shows SEM images of Sample 1–2 that indicates both pore shrinkage and deformation. The combination of pore shrinkage due to the oxygen plasma clean and minute pattern deformations created during fabrication of the photolithography mask resulted in quasi-cylindrical pores for the close-packed layouts. Because square layouts showed significantly better results, future design-fabrication cycles will avoid close-packed layouts to ensure the ideal pore geometry is maintained. Table I provides a summary of the changes that occurred to each design. A logical conclusion that can be drawn from the results shown in Table I is that samples with smaller pore sizes will experience greater amounts of pore shrinkage than samples with larger pore sizes. This trend is important to recognize during subsequent design-fabrication cycles.

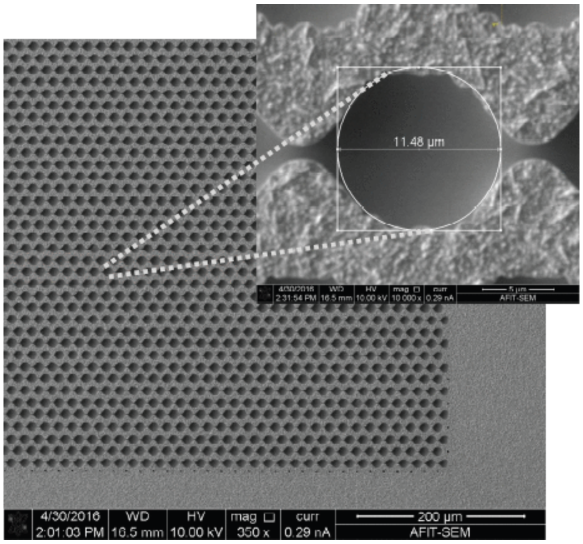

Fig. 13. Scanning electron microscope (SEM) images of sample 1–2 showing quasi-cylindrical close-packed pores.

Table I. Effects of fabrication on pore design parameters

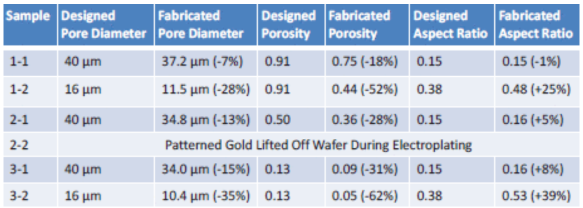

Sample	Designed Pore Diameter	Fabricated Pore Diameter	Designed Porosity	Fabricated Porosity	Designed Aspect Ratio	Fabricated Aspect Ratio
1-1	40 µm	37.2 µm (-7%)	0.91	0.75 (-18%)	0.15	0.15 (-1%)
1-2	16 µm	11.5 µm (-28%)	0.91	0.44 (-52%)	0.38	0.48 (+25%)
2-1	40 µm	34.8 µm (-13%)	0.50	0.36 (-28%)	0.15	0.16 (+5%)
2-2	Patterned Gold Lifted Off Wafer During Electroplating					
3-1	40 µm	34.0 µm (-15%)	0.13	0.09 (-31%)	0.15	0.16 (+8%)
3-2	16 µm	10.4 µm (-35%)	0.13	0.05 (-62%)	0.38	0.53 (+39%)

SECTION V. Conclusion

This effort provided a unique surface micromachining process for fabricating porous surfaces to control the SEY of a material for multipactor suppression. A mathematical analysis of an SEY model for porous surfaces was provided and led to key design rules for fabricating porous surfaces to control SEY. Porous surface designs were presented and accompanied by a fabrication process. Fabrication results were discussed and showed advantages for square layouts over close-packed layouts. The next step is to perform SEY measurements of the fabricated samples. Results will be used to validate the proposed mathematical model relating key features of the SEY curve (e.g. δ_{max}) to aspect ratio and porosity. Future work will also consist of fabrication process refinement to more precisely control pore size and shape. An additional follow-on study will seek to understand how micron-sized pores compare to nanometer-sized pores for SEY control. Such a study will likely require more innovative patterning techniques such as nanosphere lithography, electron-beam lithography, or the use of a focused ion beam, in order to create pores on the nanometer scale.

ACKNOWLEDGMENT

The authors thank the device fabrication support provided by Dr. Robert Fitch, Jason Hickey, Rich Johnson, and Adam Fritzsche.

References

1. Space engineering: Multipaction design and test, Noordwijk, 2013.

2. R. A. Kishek, Y. Y. Lau, L. K. Ang, A. Valfells, R. M. Gilgenbach, "Multipactor discharge on metals and dielectrics: Historical review and recent theories", *Phys. Plasmas*, vol. 5, no. 5, pp. 2120-2126, 1998.

3. J. R. M. Vaughan, "Multipactor", *Electron Devices IEEE Trans.*, vol. 35, no. 7, pp. 1172-1180, 1988.

4. P. T. Farnsworth, "Television by electron image scanning", *J. Franklin Inst.*, vol. 218, no. 4, pp. 411-444, 1934.

5. E. Sorolla, M. Mattes, "Multipactor saturation in parallel-plate waveguides", *Phys. Plasmas*, vol. 19, no. 7, pp. 072304, 2012.

6. S. Anza, C. Vicente, J. Gil, M. Mattes, D. Wolk, U. Wochner, V. E. Boria, B. Gimeno, D. Raboso, "Prediction of multipactor breakdown for multicarrier applications: The quasi-stationary method", *IEEE Trans. Microw. Theory Tech.*, vol. 60, no. 7, pp. 2093-2105, 2012.

7. A. J. Hatch, "Suppression of Multipacting in Particle Accelerators", *Nucl. Instruments Methods*, vol. 41, pp. 261-271, 1966.

8. F. Le Pimpec, R. E. Kirby, F. King, M. Pivi, "Electron conditioning of technical aluminium surfaces: Effect on the secondary electron yield", *J. Vac. Sci. Technol. A Vacuum Surfaces Film.*, vol. 23, no. 6, pp. 1610, 2005.

9. S. Anza, C. Vicente, J. Gil, M. Mattes, D. Wolk, U. Wochner, V. E. Boria, B. Gimeno, D. Raboso, "Prediction of multipactor breakdown for multicarrier applications: The quasi-stationary method", *IEEE Trans. Microw. Theory Tech.*, vol. 60, no. 7, pp. 2093-2105, 2012.

10. H. Bruining, Physics and Applications of Secondary Electron Emission, Elsevier Science, pp. 42-44, 1954.

11. M. Ye, Y. N. He, S. G. Hu, R. Wang, T. C. Hu, J. Yang, W. Z. Cui, "Suppression of secondary electron yield by micro-porous array structure", *J. Appl. Phys.*, vol. 113, no. 7, pp. 74904, 2013.

12. V. Nistor, L. A. Gonzalez, L. Aguilera, I. Montero, L. Galán, U. Wochner, D. Raboso, "Multipactor suppression by micro-structured gold/silver coatings for space applications", *Appl. Surf. Sci.*, no. 0, Jan. 2014.

13. O. Hachenberg, W. Brauer, "Secondary Electron Emission from Solids", *Advances in Electronics and Electron Physics*, vol. XI, pp. 413-499, 1959.